ELSEVIER

Contents lists available at ScienceDirect

## Additive Manufacturing

journal homepage: www.elsevier.com/locate/addma





# Concurrent characterization of compressibility and viscosity in extrusion-based additive manufacturing of acrylonitrile butadiene styrene with fault diagnoses

David O. Kazmer<sup>a,\*</sup>, Austin R. Colon<sup>a</sup>, Amy M. Peterson<sup>a</sup>, Sun Kyoung Kim<sup>b</sup>

#### ARTICLEINFO

Keywords: Material extrusion Viscosity Compressibility Characterization Instrumentation

#### ABSTRACT

Compressibility and viscosity of polymer feedstock are critical to their volumetric flow rate, weld strength, and dimensional accuracy in material extrusion additive manufacturing. In this work, the compressibility and viscosity of an acrylonitrile butadiene styrene (ABS) material is characterized with an instrumented hot end design. Experiments are first performed with a blocked nozzle to characterize the compressibility behavior. The results closely emulate the pressure-volume-temperature (PVT) behavior of a characterized generic ABS. Experiments are then performed with an open nozzle over a range of volumetric flow rates and temperatures. The static pressure data is fit to power-law, Ellis, and Cross viscosity models and the dynamic melt pressure data is then used to jointly fit material constitutive models for compressibility and viscosity. The results suggest that the joint fitting substantially improves the fidelity relative to the separately characterized viscosity and compressibility. The implemented methods support material extrusion process simulation and control including real-time identification of process faults such as (1) limited melting capacity of the hot end, (2) skipping (grinding) of the extruder drive gears, (3) low initial nozzle temperature, (4) varying flow rates associated with the intermeshing gear tooth velocity profile, and (5) delays and reduced melt pressures due to drool prior to extrusion. The ability to monitor the printing process for faults in real time, such as that presented in this work, is critical to born qualified parts. Additionally, these approaches can be used to screen new materials and identify optimal processing conditions that avoid these process faults.

#### 1. Introduction

Material extrusion, also referred to as fused filament fabrication (FFF) and fused deposition modeling (FDM), is an additive manufacturing technique that deposits roads of molten polymer that solidify into a desired shape. Material extrusion enables the creation of complex designs without tooling that are difficult to produce or otherwise unattainable via traditional manufacturing.

Despite its widespread use and extensive related research, compressibility effects have not been widely studied in material extrusion. The apparent reason is that melt pressures are low, on the order of 1 MPa, and so intuition would suggest that compressibility effects are not very significant. As such, it is not surprising that pre-processors (slicers) assume incompressibility when calculating extruder move commands. Specifically, conservation of volume is assumed such that

the extruder flow rate,  $Q_E$ , is equal to the flow rate during deposition, WHS, where W is the road width, H is the road height, and S is the print speed. The process then operates in an open loop mode wherein the input material driven by the stepping of a feed gear is assumed proportional to the output at the nozzle orifice.

However, the bulk modulus of the material in view of the operating pressure and desired precision suggests that compressibility effects can be significant. For example, consider a filament having a diameter, D, of 1.75 mm that is used with an extruder having a transmission providing  $n=340\,$  steps/mm. The volume,  $V_{\rm Step}$ , associated with each step is  $(\pi D^2/4)(1\,{\rm mm/n})$  equal to  $0.007\,{\rm mm}^3$  By comparison, consider the compression of polymeric materials having an isothermal compressibility,  $\beta$ , of  $1\cdot10^{-2}\,{\rm MPa}^{-1}$  (equal to  $1/b_3$  as later detailed in Table 1 [1]) that is exposed to a melt pressure P of 1 MPa on a length L of 79 mm between the extruder and the nozzle orifice. The volume change,  $V_{\rm C}$ , due

E-mail address: David Kazmer@uml.edu (D.O. Kazmer).

<sup>&</sup>lt;sup>a</sup> Department of Plastics Engineering, University of Massachusetts Lowell, Lowell, MA 01854, USA

b Seoul National University of Science and Technology, Department of Product Design and Engineering, Seoul 01811, South Korea

<sup>\*</sup> Corresponding author.

Table 1

Double-domain Tait equation coefficients for generic ABS [1].

Coefficient	Solid	Melt
$b_{1,.}$ (m <sup>3</sup> /kg)	9.829e-4	9.829e-4
$b_{2,}$ . (m <sup>3</sup> /kg K)	3.061e-7	6.504e-7
b <sub>3,</sub> . (Pa)	2.41941e+8	1.140e+8
b <sub>4,</sub> . (1/K)	4.001e-3	4.919e-3
b <sub>5</sub> (K)	376.75	
b <sub>6</sub> (K/Pa)	2.377e-7	

to material compression going from 0 pressure to P is  $(\pi D^2 L/4)(\beta P)$  equal to 1.90mm³ The change in volume due to pressurization of the melt is thus a significant amount of displacement relative to the motor stepping and should be accounted for whenever the extruder starts, stops, or changes velocities.

A non-Newtonian, compressible flow model-based AM extrusion process controller is envisioned that ties the transient input from the extruder not only to the states during material extrusion but also to the post-deposition material states and ultimately the printed part properties. The approach is inspired by the work of Chiang, Hieber, Wang, and others who proposed and realized a unified simulation for filling and postfilling stages of injection molding [2,3] during the Cornell Injection Molding Program (CIMP). To support such future process control, this paper jointly models the viscosity and compressibility of using transient melt pressure data from an instrumented hot end in extrusion-based

additive manufacturing. While the methods are relatively simple, the results provide a reasonable and useful representation of the dynamic material behavior.

#### 2. Experimental

To measure the pressure in the hot end during operation for characterization of viscosity and compressibility, hot ends were manufactured to transmit the melt pressure at a slit within the hot end to a mounted load cell. The custom instrumented hot end is shown in Fig. 1. The hot end differs from prior designs of Coogan and Kazmer [4,5] in moving the melt sensor from the nozzle tip to the body of the hot end. The primary motivation in the redesign was to improve the robustness of the instrumentation while allowing the use of standard, interchangeable nozzles. In detailing the design, it was recognized that the incorporation of a flow channel within the hot end in the form of a slit would allow the use of a larger pressure sensing pin while allowing the sensing surface of the pin to remain parallel with the surface of slit wall, thereby avoiding melt interference. The larger pressure sensing pin allows for a surface area of the melt proportional to the squared diameter with a circumferential area proportional to the diameter, thereby increasing the signal to noise ratio of the sensor through an increase in applied force as well as a reduction of relative drag effects.

The dimensions of the melt sensor pin and the bore of the hot end were designed for a tight sliding fit. Hot ends were produced in cast brass and bronze via 3D printed SLA patterns as well as in stainless steel 316 by powder bed fusion. In both cases, the bore of the hot end's sensor port

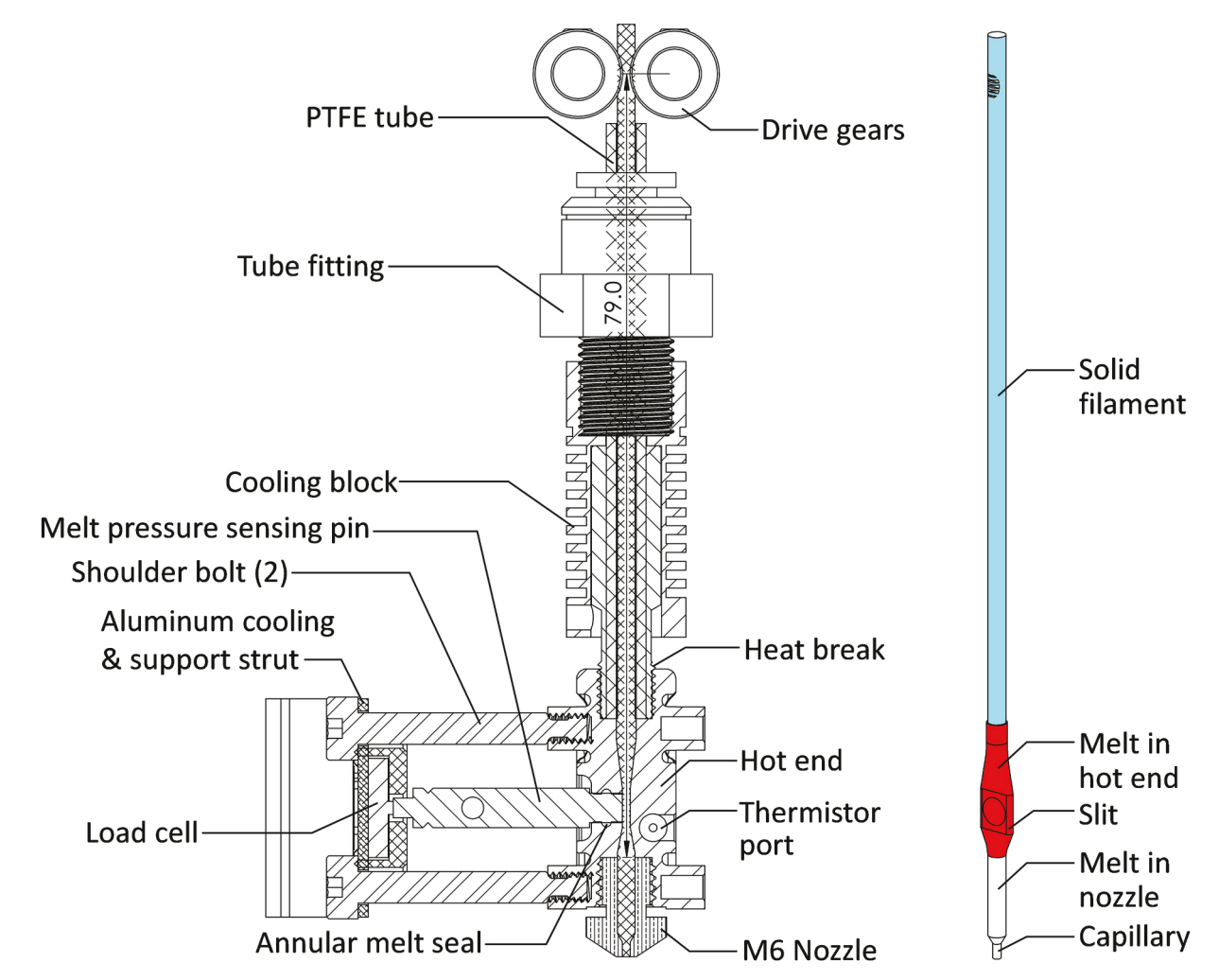


Fig. 1. (a, left) Section view of instrumented hot end, (b, right) isometric view of feedstock.

was designed to have a nominal diameter of 2.9 mm, then drilled to a nominal diameter of 2.95 mm, then reamed to a finished diameter of 3.00 mm. The diameter of the melt sensor pin was turned on a lathe to a nominal diameter of 2.98 mm. In operation, no leakage of the material being processed was observed after several hours of characterization and printing at varying processing conditions. One reason for the minimal leakage may be that the nominal radial clearance of 0.01 mm between the melt sensor pin and bore of the hot end is suitable for this material and process. Another reason is that the side wall of the hot end receiving the melt sensor pin was provided an annulus with a width and thickness of 1 mm that tends to provide a dynamic melt seal by helping to center the sensor pin while also providing lower shear rates and higher viscosities in the micro-gap [6] surrounding the pin.

In the design of Fig. 1, shoulder bolts are used to locate and attach the cooling/support strut to the hot end. To minimize mass, an extruded aluminum low profile strut channel was found to provide sufficient stiffness and excellent heat transfer for cooling of the load cell. PEEK washers between the shoulder bolts and hot end were used to adjust the axial position of the support strut so that the load cell was not in compression by the melt sensor pin when not under load. The implemented load cell was an Aloce GB/T7561-2009 (Xi'an Gavin Electronic Technology Co, Xi'an, Shaanxi, China) with a rated load capacity of 10 kgf, compensated temperature range of − 10 to 60 °C, operating temperature range of -20 to 80  $^{\circ}$ C, comprehensive error less than 0.1% of full scale load, and creep less than 0.05% of full scale load across 30 min. The rated output is 0.91088 mV/V with a 5 VDC excitation. Data from the load cell was amplified and converted to a digital signal with a load cell signal conditioner (Sparkfun P/N SEN-15242) that includes a NAU7802 (Nuvoton, Taiwan) 24-bit analog to digital convertor for the strain gage. The load cell signal was acquired as a digital signal from the conditioner by an Artemis OpenLog microcontroller (Sparkfun P/N DEV-16832) as a scan rate of 78 Hz. The 10 kgf load capacity for the 3 mm diameter pin corresponds to a maximum melt pressure of 13.9 MPa, and theoretical pressure resolution of 0.2 kPa a 16 bit pressure signal. In practice, the authors reliably observed minimum melt pressures on the order of 0.01 MPa with noise on the order of 0.002 MPa.

The instrumented hot end was operated with a Creality Ender 5 printer. The printer was unmodified except for the instrumented hot end and the use of a direct drive extruder (Micro Swiss P/N M2601, Ramsey, MN) designed with 79 mm of filament length between the extruder drive gears and the bottom of the hot end. The 79 mm length as well as the 340 steps/mm used in the example of the introduction correspond to this experimental setup. The solid filament was constrained within a PTFE tube having a 2 mm bore and 4 mm outer diameter; the PTFE tube was itself supported by the heat break, cooling block, and tube fitting as shown in Fig. 1. An acrylonitrile butadiene styrene polymer (Hatchbox ABS, red, 1.75 mm diameter) was processed at temperatures of 160, 180, 200, 220, and 240 °C for characterization purposes. The hot end temperatures were maintained by the printer's closed loop control in response to a feedback signal from a 100  $k\Omega$  thermistor inserted into the hot end's thermistor port. The process was monitored, and temperatures were observed to reside within 1 °C of the set-point after the process equilibrated.

## 3. Modeling and characterization of compressibility

The specific volume  $\nu$  is well characterized by the pressure-volume-temperature (PVT) relations according to the Tait equation. The Tait equation was originally derived to model the density of fresh and sea water over wide pressure ranges [7–9], and has since been found to accurately predict the specific volume of dense gases, liquids, solids, and mixtures. Zoller designed an instrument for characterizing the PVT behavior of polymers and modeling this behavior with the double domain Tait equation [10–12]. Here, the term "double domain" means that the specific volume is modeled separately in the solid and melt

states as a function of pressure and temperature:

$$v(T, P) = v_0(T) \left(1 - 0.0894 ln \left(1 + \frac{P}{B(T)}\right)\right) + v_T(T, P)$$
 (1)

The transition temperature between the solid and melt states is modeled as a function of pressure as:

$$T_T(P) = b_5 + b_6 P (2)$$

For temperatures above the transition temperature, the reference specific volume,  $v_0(T)$ , and bulk modulus, B(T), are modeled as [10–12]:

$$v_0(T) = b_{1,m} + b_{2,m}(T - b_5)$$
(3)

$$B(T) = b_{3,m} exp(-b_{4,m}(T - b_5))$$
(4)

The coefficient  $b_5$  is the transition temperature at zero pressure, and  $b_6$  is the rate of change of the transition temperature with respect to pressure. For temperatures below the transition temperature, the reference specific volume and compressibility are similarly modeled albeit with a different set of coefficients. The term  $v_T$  in Eq. (1) represents the additional specific volume associated with the transition volume of semi-crystalline polymers, and is 0 for amorphous polymers such as ABS. In theory, the transition volume could be modeled if the material could be characterized at lower temperatures. With the current setup, however, these lower temperatures cause material solidification that prevents pressure transmission to the melt sensor pin.

For comparison with the presented results, the PVT behavior from the double-domain Tait equation is provided in Fig. 2 for a generic ABS material while the fitted model coefficients in its solid and melt state are provided in Table 1. This generic ABS material is provided in the Autodesk/Moldflow database [1] and intended for use when the specific grade of ABS is unknown. Inspection of Fig. 2 indicates that the specific volume increases with temperature (thermal expansion) and decreases with pressure (compression). Moreover, it is observed that there is greater compressibility at elevated melt temperatures, meaning that compressibility effects are more significant in the material in the hot end than in the cooler filament between the hot end and extruder.

The characterization of compressibility with the instrumented hot end follows directly from the definition of compressibility given the observed pressure in response to applied compression on a known volume:

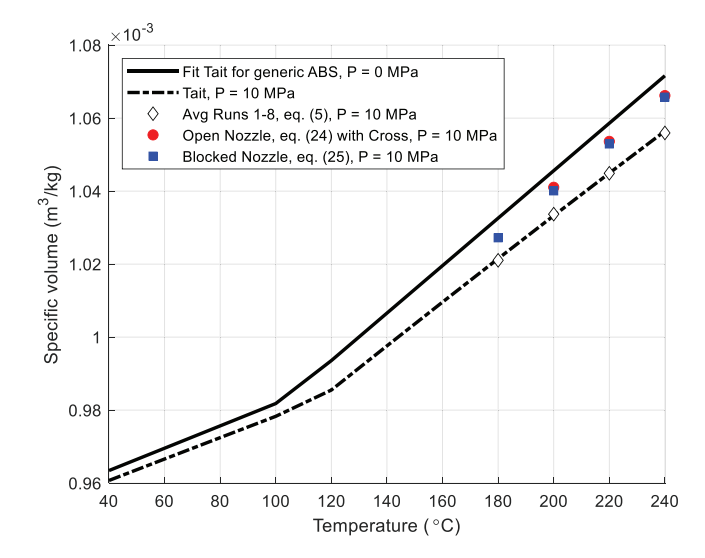


**Fig. 2.** Specific volume as a function of temperature and pressure (PVT behavior) of generic ABS according to the double-domain Tait equation coefficients of Table 1 as well as later discussed results of characterized ABS according to Tables 3 and 6 (jointly fit with Cross model).

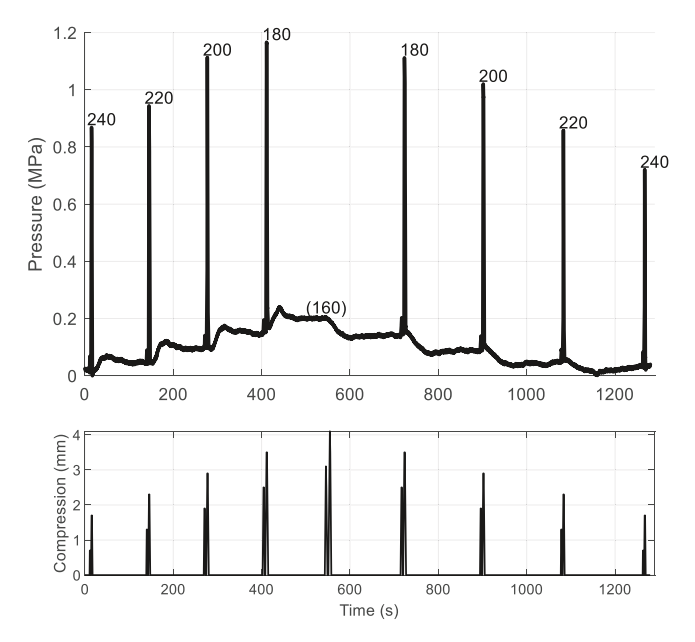


Fig. 3. (bottom) Applied compression by extruder, and (top) observed melt pressure responses as measured in the instrumented hot end of Fig.  $1.^{21}$  Labeled values on the top graph indicate extruder temperature settings in degrees Celsius.

$$\beta(T) = -\frac{1}{V} \frac{dV}{dP} \Big|_{T} = -\frac{1}{V} \frac{\Delta V}{\Delta P}$$
 (5)

To impose compression of  $\Delta V$ , the nozzle of the instrumented hot end was replaced with a solid plug in the form of an M6 bolt. While the slit geometry is not circular, it was designed so that its cross-section area equals the cross-section area of the filament. The loft between the circular filament and the slit likewise has nearly the same cross-section area of the filament. The volume of the material between the drive gears and the plug is then well-estimated as  $V = \pi/4D^2L$  or  $190.0 \text{mm}^3$ . The methodology to test the compressibility of the material was:

- Set the hot end temperature to a target set temperature, T, of 240 °C;
- Allow the system to reach the set temperature, then equilibrate for two minutes:
- Advance the material to provide 1.3% compression and hold for 1 s;
- Retract the material to decompress the material and hold for 1 s;
- Advance the material to provide 2.6% compression and hold for 1 s;
- Retract the material to decompress the material and hold for 1 s;
- Repeat for decreasing temperatures of 220, 200, 180, and 160 °C; and,
- Repeat for increasing temperatures of 180, 200, 220, and 240 °C.

It is important to note that the PVT behavior of Fig. 2 indicates a significant coefficient of thermal expansion relative to the

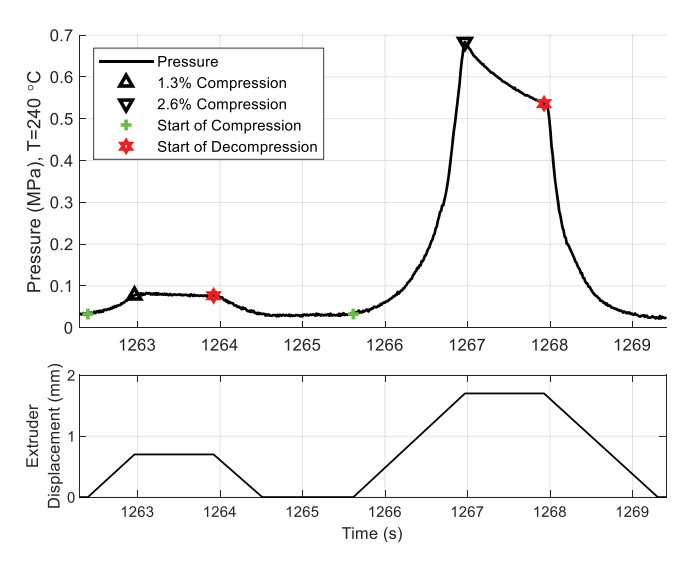


Fig. 4. (top) Observed pressure and (bottom) extruder displacement given 1.3% and 2.6% compression at set temperature of 240  $^{\circ}$ C.

compressibility. As such, it is important to compensate for the changes in the specific volume with changes in the set temperatures. This compensation is performed to define the extruder's offset position,  $E_O$ , that is applied in addition to low and high compression for each set temperature, T, as:

$$E_O(P=0) = -(T - T_{Max})(V(T, P) - V(T_T, P))/(T_{Max} - T_T)/A$$
 (6)

where  $T_{Max}$  is the maximum characterization temperature of 240 °C and A is the cross-section area of the filament. The applied extruder displacements and observed pressures from the instrumented hot end are plotted in Fig. 3; the data set consisting of 97,338 rows of set extruder positions and observed pressures are provided as supplemental material 1a. In Fig. 3, it is observed that there are impulse responses in the melt pressure for all the set temperatures except for 160  $^{\circ}$ C. For the 160  $^{\circ}$ C setting, it is believed that the ABS material was too cold in the section of the hot end adjacent the heat break to transmit stress to the sensor pin. Each of the other eight temperatures exhibits a small initial impulse response corresponding to the application of the 1.3% compression followed by a much larger impulse response upon application of the 2.6% compression. In Fig. 3, an offset in the observed no-load pressure is observed with changes in temperature. This no-load pressure is likely due to the temperature sensitivity of strain gages in the load cell. However, it should not affect the compressibility modeling since the analysis is based on the relative change in the pressure between the low and high compression states.

The applied compression and resulting pressure for the final characterization at 240  $^{\circ}$ C is shown in Fig. 4; all eight responses were generally similar in behavior and are plotted in supplemental material 1b. At time 1262.3 s in Fig. 4, the extruder begins to compress the material by linearly advancing the filament at a rate of 1 mm/s to 1.3%

 $<sup>^1</sup>$  Without this extruder offset, the volumetric shrinkage could be so significant that no compressive stress (melt pressure) would be observed when applying the same extruder displacements at lower melt temperatures. Conversely, the same extruder displacements that work at lower melt temperatures could result in melt pressures that exceed the 13.9 MPa design limit if applied at higher temperatures. As the later results indicate, the selection of the offset and subsequent extruder displacements that worked well as the low limit was large enough to accommodate errors in the estimation of  $\nu_0(T)$  based on  $b_{1,\mathrm{m}}$  and  $b_{2,\mathrm{m}}$ . This research is motivated to characterize  $b_{3,\mathrm{m}}$  and  $b_{4,\mathrm{m}}$  but it is likely that  $b_{1,\mathrm{m}}$  and  $b_{2,\mathrm{m}}$  could also be estimated by using different extruder displacement strategies.

**Table 2**Observed pressures estimated isothermal compressibility and bulk modulus for the pressure data plotted in Fig. 3.

Run	T (°C)	$P_1$ , std (MPa)	$P_2$ , std (MPa)	$\Delta P \text{ (MPa)}$	$\beta$ (Pa <sup>-1</sup> )	B (Pa)
1	240	0.0651, 0.0016	0.8917, 0.0014	0.8266	1.531e-08	6.529e + 07
2	220	0.0833, 0.0008	0.9338, 0.0156	0.8505	1.488e-08	6.719e + 07
3	200	0.1315, 0.0014	1.1096, 0.0301	0.9780	1.294e-08	7.726e + 07
4	180	0.1866, 0.0011	1.1707, 0.0109	0.9841	1.286e-08	7.774e + 07
5	180	0.1878, 0.0011	1.1028, 0.0031	0.9150	1.383e-08	7.228e + 07
6	200	0.1156, 0.0019	1.0013, 0.0247	0.8857	1.429e-08	6.997e + 07
7	220	0.0820, 0.0022	0.8546, 0.0025	0.7726	1.638e-08	6.103e + 07
8	240	0.0773, 0.0023	0.6751, 0.0116	0.5978	2.117e-08	4.722e + 07

compression (volume of  $1.68~\rm mm^3$  given a filament diameter of  $1.75~\rm mm$ ). The observed pressure slowly begins to rise to  $0.0773~\rm MPa$  at a time of  $1263~\rm s$ . The filament is then held at that position for  $1~\rm s$  and is then retracted and remains at rest for  $1~\rm s$ . At a time of  $1265.6~\rm s$ , the extruder linearly advances the filament at a rate of  $1~\rm mm/s$  to 2.6% compression (volume of  $4.09~\rm mm^3$ ) and the pressure rises to  $0.684~\rm MPa$ . While the filament is subsequently held in compression, it is observed that the pressure decays to  $0.531~\rm MPa$ . The authors believe that this melt pressure decay is not due to leakage or viscoelastic response of the melt but rather cooling and related volumetric shrinkage of the adiabatically heated material upon compression.

Table 2 summarizes the magnitude of the pressure impulses plotted in Fig. 3 where  $P_1$  and  $P_2$  respectively correspond to the 1.3% and 2.6% compression (e.g., corresponding to 1263 and 1267 s in Fig. 4). The standard deviation data (std) are calculated from the seven pressure readings centered about the reported pressure; the standard deviation data indicates that the pressures used for calculating the compressibility are relatively stable with greater variation pressure at higher

$$\frac{dT}{dP} = \left(\frac{d\nu}{dP}\right) / \left(\frac{d\nu}{dT}\right) = -\frac{\beta}{\alpha}$$

This concept was recently used to design high performance extrusion screws by leveraging melt decompression in the metering zone to manage shear heating by melt decompression (see [13] D. O. Kazmer, C. M. Grosskopf, D. Rondeau, and V. Venoor, "Design and evaluation of general purpose, barrier, and multichannel plasticating extrusion screws," Polymer Engineering & Science, vol. 60, no. 4, pp. 752-764, 2020.) As described there, the coefficients  $\alpha$  and  $\beta$  are readily estimated by the Tait equation of state. For polymers, the temperature sensitivity with respect to pressure, dT/dP, is around 1.5 °C/MPa. The resulting temperature increase in the material upon sudden application of compression as shown in Fig. 3 would therefore increase the pressure more than otherwise expected. Furthermore, the exponential decay of the pressure is also indicative of an exponential decay in temperature, which follows from the solution of the heat conduction equation for a prismatic object. For polymers, a good approximation of the characteristic cooling time is  $\tau = 2[s/mm^2] \times (H[mm])^2$  where H is the wall thickness of the object (see [14] D. Kazmer, Injection mold design engineering, 2nd edition. Munich: Carl Hanser Verlag, 2016, p. 410.) In the hot end design, the slit thickness of 0.8 mm results in a characteristic cooling time of 1.28 s, which approximates the time response of the pressure decay seen in Fig. 4.

compression as expected given the higher pressure and derivative,  $dP_2/dt$ . The isothermal compressibility is then calculated by definition of Eq. (5) as  $\beta=P_2/\varepsilon$  given  $\varepsilon=\Delta V/V$ . The bulk modulus is calculated as  $B=1/\beta$  and is useful for fitting  $b_{3,\mathrm{m}}$  and  $b_{4,\mathrm{m}}$  of Eq. (3) by multiple regression.

Table 3 provides the fitted Tait model coefficients  $b_{3,m}$  and  $b_{4,m}$  to model the bulk modulus as a function of temperature according to Eq. (3). Model 1 repeats the  $b_{3,m}$  and  $b_{4,m}$  Tait model coefficients for the generic ABS material from Table 1 [1]. Model 2 provides the  $b_{3,m}$  and  $b_{4,m}$  coefficients for the first four runs when the hot end temperatures are decreasing while model 3 provides the same coefficients for the last four runs when the hot end temperatures are increasing. Model 4 provides the  $b_{3,m}$  and  $b_{4,m}$  coefficients fitted to all eight runs with very close agreement to the Tait model as plotted in Fig. 2 for an applied pressure of 10 MPa.

While the results have statistically significant coefficients that generally agree with the fitted Tait model coefficients, this approach using a blocked nozzle is academically interesting but practically useless since the blocked nozzle itself precludes the use of the extruder for additive manufacturing. It is true that the blocked nozzle may be used for characterization and then replaced with a traditional nozzle, but such an approach still precludes the in-line characterization of compressibility during AM. The authors are thus motivated to pursue the concurrent characterization of compressibility with viscosity, which leads to the next section on incompressible modeling of the apparent viscosity based on steady state flow. Afterwards, the joint modeling of viscosity and compressibility is developed based on transient flow behavior, which provides the very different result on model 5 in Table 1.

## 4. Incompressible modeling and characterization of viscosity

An experiment was conducted to characterize the flow behavior of the ABS being processed at  $T_j = \{240, 220, 200\}[^{\circ}C]$  and step changes in flow rates. To avoid excess melt pressure at high flow rates and low temperatures, the flow rates  $Q_i^j$  were varied from according to the formula:

$$Q_i^j = 20 \times 2^{-(i-j)/2} \tag{7}$$

where  $j \in \{1, 2, 3\}$  represents the index for the temperature setting and i represents the index for the flow rate ranging from 1 to 20. The flow rates were imposed for 5 s after which the extruder was stopped and held for 5 s; no retraction was applied so the material was free to decompress and drool from the nozzle. The data set consisting of 50,889 rows of set temperatures, set flow rates, and observed flow rates are provided in the supplemental materials. The tested flow rates are provided in the lower subplot of Fig. 5 with the melt pressure responses provided in the upper subplot. As shown, a rise in the melt pressure followed by melt pressure decay is observed for each step application of the flow rate from 20 to 0.3 mm<sup>3</sup>/s at 240 °C, 14.1–0.16 mm<sup>3</sup>/s at 220 °C, and 10–0.11 mm<sup>3</sup>/s at 200 °C. Below the indicated flow rates, melt pressures were not observable. Accordingly, the experiment resulted in a set of 39 runs with observable melt pressures at varying

<sup>&</sup>lt;sup>2</sup> Close inspection of the time span between traces indicates that the settling time for cooling ( $t_C$ , circa 100 s) is longer than the settling time for heating ( $t_H$ , circa 30 s). Given the use of a 30 W cartridge heater that provides heating power,  $P_H$ , while cooling power,  $P_C$ , is also being applied via a cooling fan. For those interested, the effective cooling power can be estimated from the solution of the equation  $P_H t_H + P_C t_H = P_C t_C$  as 13 W.

<sup>&</sup>lt;sup>3</sup> Since the specific volume is both a function of pressure *P* and temperature *T*, calculus suggests that the equation of state can be used to provide an estimate of the response of temperature with pressure:

**Table 3**Estimated Tait model coefficients from the bulk modulus data of Table 2.

Model	Coefficient	Estimate	SE	t-statistic	p-value
1. Tait model,Eq. (3) (Table 1)	b <sub>3,m</sub> (Pa)	1.140e+8	n/a	n/a	n/a
	$b_{4,m}$ (1/K)	4.919e-3	n/a	n/a	n/a
2. Runs 1–4,Eq. (5) $R^2 = 0.869$	b <sub>3,m</sub> (Pa)	1.016e + 8	1.426e-14	7.123e+21	6.101e-66
	$b_{4,m}$ (1/K)	3.282e-3	1.562e-4	21.02	2.356e-4
3. Runs 5–8,Eq. (5) $R^2 = 0.879$	b <sub>3,m</sub> (Pa)	1.232e + 8	2.369e-14	5.200e+21	1.568e-65
	$b_{4,m}$ (1/K)	6.460e-3	3.054e-4	21.16	2.311e-4
4. Average Runs 1–8,Eq. (5) $R^2 = 0.915$	b <sub>3,m</sub> (Pa)	1.112e + 8	1.543e-14	7.212e+21	5.879e-66
	$b_{4,m}$ (1/K)	4.789e-3	1.824e-4	26.26	1.212e-4
5. Ave Runs 1–8,Eq. (25) $R^2 = 0.551$	b <sub>3,m</sub> (Pa)	1.763e + 8	4.244e-15	4.156e22	3.071e-68
	$b_{4,{\rm m}}~(1/{\rm K})$	7.593e-4	8.250e-5	9.204	2.713e-3

temperatures,  $T_i$ , and flow rates,  $Q_i^j$ .

Fig. 6 plots the same melt pressure data as in the top subplot of Fig. 5, but with a logarithmic scale for the melt pressure as well as a time offset to superimpose the flow rate steps. The melt pressure data was not filtered after acquisition, though it is noted that the data acquisition system in the implemented Artemis OpenLog microcontroller (Sparkfun P/N DEV-16832) applied a default four sample averaging filter. Regardless, the data is very rich with respect to revealing the material behavior and so is provided in supplemental material 2a. Generally, each application of a step flow rate causes a response in the melt pressure with a behavior similar to  $1 - \exp(-t)$  after which the cessation of the flow causes a decrease in the melt pressure with a behavior similar to  $\exp(-t)$ . There are some significant and interesting variations that are not readily apparent given the limited resolution of this figure but are later discussed in more detail.

Given this pressure and flow rate data, the apparent viscosity as a function of shear rate may be directly calculated assuming incompressibility. Specifically, the wall shear rate,  $\dot{\gamma}$ , and viscosity,  $\mu$ , are estimated for a Newtonian fluid as:

$$\dot{\gamma} = 4Q/(\pi R^3) \tag{8}$$

$$\mu = \pi P R^4 / (8LQ) \tag{9}$$

where R is 0.2 mm and L is 1 mm for the stock nozzle of the Creality Ender 5. Fig. 7 plots the apparent viscosity as a function of shear rate derived from the pressure and flow rate data of Fig. 5 for the characterized ABS. Vertical error bars representing the standard deviation of

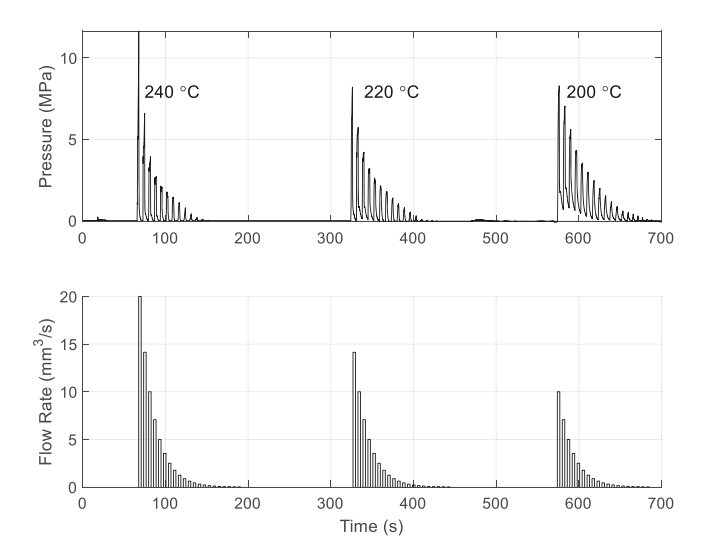


Fig. 5. (bottom) imposed flow rates at 240, 220, and 200  $^{\circ}\text{C}$  and (top) observed pressures.

the viscosity are provided for each observation, while observations having a coefficient of variation (COV, defined as the standard deviation divided by the mean) greater than 2% are indicated with an "x".

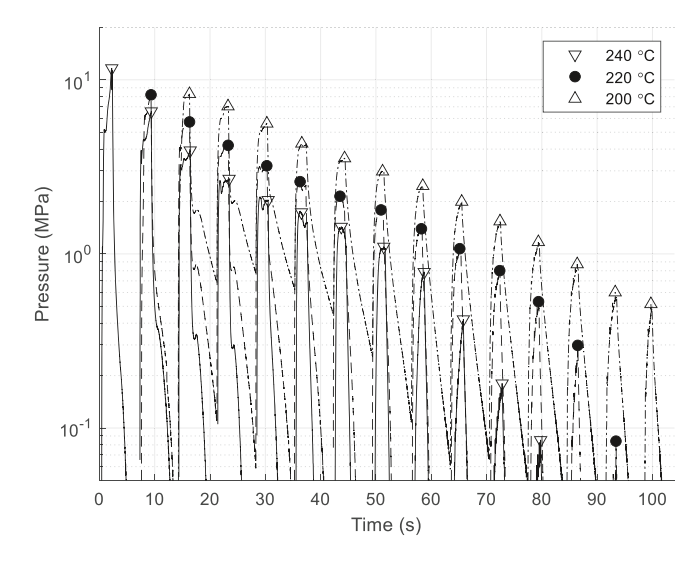


Fig. 6. Melt pressures of Fig. 5 plotted on a logarithmic scale and superimposed.

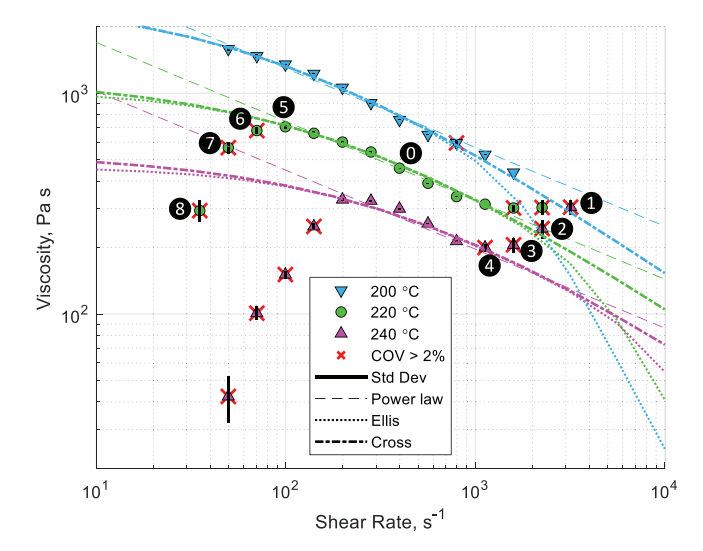


Fig. 7. Apparent viscosity as a function of wall shear rate based on peak pressures and flow rates of Fig. 5. Points marked with an "x" indicate observations having a coefficient of variation greater than 2% due to faults identified in the discussion section; numbered points are later discussed with respect to observed pressure dynamics.

**Table 4**Estimated viscosity model coefficients to the apparent viscosity data of Fig. 7.

Model	Coefficient	Estimate	SE	t-statistic	p-value
Power-law $R^2 = 0.992$ (Viscosity)	k [Pa s <sup>2-m</sup> ]	8.213e-3	0.995	1.77	0.0928
	C [K]	6440	261	24.7	1.88e-16
	m	0.6424	0.0118	54.5	3.10e-23
Ellis $R^2 = 0$ . 993 (Viscosity)	$k$ [Pa s <sup>1+<math>\alpha</math></sup> ]	1.666e-6	3.76e-8	44.3	3.13e-22
	C [K]	9974	8.52e-7	1.17e19	4.77e-199
	$ au_{1/2}$	2.051e5	1.06e-7	1.93e12	1.28e-245
	$\alpha$	2.188	0.0368	59.5	6.84e-25
Cross R <sup>2</sup> = 0.998 (Viscosity)	$k$ [Pa s <sup>1+<math>\alpha</math></sup> ]	2.073e-6	1.86e-8	111.2	1.38e-30
	C [K]	9939	5.70e-8	1.74e11	1.13e-223
	$\tau^*[Pa\ s]$	2.410e5	6.75e-9	3.57e13	3.31e-272
	n	0.4019	0.00993	40.5	2.06e-21

The accepted (viscosity, shear rate) observations of Fig. 7 are fit to material constitutive models for use in simulation and control. Three widely used models are the power-law model, the Ellis model, and the Cross model respectively provided as:

$$\eta(\dot{\gamma}, T) = k \dot{\gamma}^{m-1} \exp(C/T) \tag{10}$$

$$\eta(\tau, T) = k \exp(C/T) / \left(1 + \left(\tau/\tau_{1/2}\right)\right)^{\alpha - 1} \tag{11}$$

$$\eta(\dot{\gamma}, T) = k \exp(C/T) / (1 + (k \exp(C/T)\dot{\gamma}/\tau^*))^{1-n}$$
(12)

Each of these models has strengths and weaknesses. The power-law model requires only three coefficients and is readily integrable but tends to overpredict melt pressure given high viscosity estimates at low shear rates. The Ellis model provides a transition from a Newtonian plateau to a power law regime at a transition shear stress,  $\tau_{1/2}$ , and is also readily integrable. However, the Ellis model is expressed as a function of shear stress and has an overly broad transition range. The Cross model provides an intuitive model form with coefficients that are readily estimable from a viscosity-shear rate graph and is straightforward to calculate but is not easily integrable (though analytical solutions do exist and are applied in the next results section.) While each of these models is fitted with an Arrhenius temperature dependence, a Williams-Landel-Ferry (WLF) temperature dependence [15,16] could also be implemented.

Each of the models was fitted to the apparent viscosity-shear rate data of Fig. 7 using the Matlab function fitnlm(). The results of the model fitting are provided in Table 4, and the models' behaviors are also plotted in Fig. 7. It is observed that each of the models provides a reasonably good fit to the observed data, though there are some significant differences in the viscosity behavior as a function of shear rate. Generally, the power-law model provides a reasonable estimate through the center of the data but tends to overpredict the viscosity at both low and high shear rates. The reason for the overprediction at low shear rates is that the power-law model does not model the Newtonian plateau. At the same time, the power-law model provides a relatively high powerlaw index (favoring the Newtonian limit) and so overpredicts the viscosity at high shear rates. By comparison, both the Ellis and Cross models provide reasonable modeling of the of the Newtonian plateau and initial transition to the power-law regime. However, the Ellis model provides a varying slope of the viscosity at higher shear rates since the model behavior is governed by the transition shear stress and not shear rate.4 These variances in model behaviors are reflected by the

coefficients of determination, R<sup>2</sup>, with the Cross model providing the desired topology while also statistically explaining most of the observed variation in the viscosity as a function of shear rate.

The foregoing characterization of the viscosity relies on the pressure behavior to each step response in flow rate; such an approach is common in capillary rheometry to characterize the apparent viscosity. However, examination of transient pressures plotted in Fig. 6 indicates that the behavior does not approach steady state in many of the investigated temperature and flow rate conditions. While the viscosity models are still useful, the analysis identifies excursions in the apparent viscosity as a function of shear rate as indicated in Fig. 7. The transient startup and decay behavior after each step change in flow rate is primarily due to compressibility. Rather than discard this data, the next section models the transient compressible flow behavior. This higher fidelity modeling then provides insights into some of the excursions of Fig. 7 that are not due to compressibility with subsequent discussion of fault diagnosis.

### 5. Concurrent modeling of viscosity and compressibility

The results of the two foregoing sections suggest that the compressibility and viscosity behavior of materials being processed can be separately characterized using the instrumented hot end with blocked and open nozzles. The goal of this section is to model the compressible flow in the system as a function of the varying pressures observed in Fig. 6 to concurrently characterize both the viscosity and compressibility of the material. If possible, then any candidate material could be characterized in situ to (i) identify the suitability and consistency of the material relative to expectations, (ii) adjust the nominal print settings such as temperatures and print speed to ensure process feasibility, or (iii) adjust the print speeds in real time to compensate for compressibility effects and optimize and assure the printed product quality.

Mitsoulis [17] previously investigated compressibility phenomenon for linear low-density polyethylene (LLDPE) in capillary rheometry, but did not actually use the data to jointly fit compressibility and viscosity model coefficients. Our implemented approach decomposes the extruder mass flow rate,  $\dot{m}_E$ , into two components consisting of the outlet mass flow rate,  $\dot{m}_O$ , and the internal fluid capacitance due to compressibility,  $\dot{m}_C$ :

$$\dot{m}_E(t) = \dot{m}_O(t) + \dot{m}_C(t) \tag{13}$$

The extruder mass flow rate is estimated from cross section, A, of the filament together with the extruder feed rate, F = dE/dt, and the specific volume,  $\nu_0$ , taken at ambient temperature,  $T_0 = 40$  °C, and pressure,  $P_0 = 0$  MPa:

$$\dot{m}_E(t) = A(dE(t)/dt)/v_0(P_0, T_0)$$
 (14)

The specific volume,  $v_0$ , of the incoming material is considered constant since the filament located above the feed gears is at ambient temperature and not under stress until secured by the blades of the feed gear;  $v_0$  is estimated as 0.9634 mL/g from the PVT model and coefficients of Table 1. Subsequently, the specific volume of the material

<sup>&</sup>lt;sup>4</sup> Viscosity estimation with the Ellis model is obtained by iteratively evaluating the viscosity and shear stress at a given shear rate until the viscosity converges. The issue of the viscosity cross-over in the shear thinning regime with the Ellis model can be resolved by expressing the critical shear stress,  $\tau_{1/2}$ , as a function of temperature reflecting the role of time-temperature superposition in the shear thinning behavior.

below the feed gear is modeled as a function of the pressure and temperature recorded for the hot end. For the sake of simplicity, the entirety of the material in the system (between the feed gear and the final nozzle bore) is modeled at constant pressure and temperature. This approach should provide a reasonable estimate of the compressible behavior but underestimate the compressibility of the material since a large section of the filament (approximately 55 of the 79 mm length of the instrumented hot end shown in Fig. 1) is maintained at lower temperatures than the hot end and so is less compressible. For system control purposes, however, such a lumped parameter model is acceptable and even desirable since it provides the simplest possible representation of the combined system behavior [18].

The compressible flow rate (fluid capacitance) due to fluctuating pressure may be estimated by applying the chain rule  $Q_C = d\nu_C/dt = (d\nu_C/dP)(dP/dt)$  to Eq. (2), which results in

$$\dot{m}_C(t) = \beta V_{\text{Feed}}(dP(t)/dt)/\nu(P(t), T(t))$$
(15)

where the specific volume is calculated according to Eqs. (1)–(3). Examination of Eq. (1) indicates that changes in the specific volume are governed by the bulk modulus, B(T). As such, the coefficients  $b_{3,m}$  and  $b_{4,m}$  for compressibility are fitted concurrently with the viscosity model coefficients to minimize the sum of squared error, *SSE*:

$$SSE = \sum_{t} e(t)^2 \tag{16}$$

where the error is defined as the difference between the mass flow rate from the extruder and the sum of the outlet mass flow rate and fluid capacitance:

$$e(t) = (\dot{m}_E(t) - (\dot{m}_O(t) + \dot{m}_C(t)))$$
(17)

The outlet mass flow rate,  $\dot{m}_{O}$ , is estimated from the estimated volumetric flow rate,  $\hat{Q}(P(t))$ , and the specific volume in the nozzle hore:

$$\dot{m}_O(t) = \widehat{Q}(P(t)) / \nu \left(\overline{P}(t), T(t)\right)$$
(18)

where  $\overline{P}(t)$  is the average pressure of the melt located in the bore of the nozzle tip having radius R=0.2 mm and length L=1 mm. The average melt pressure is assumed equal to half of the observed pressure, P(t), given a linear pressure gradient along the nozzle bore. The estimated flow rate is calculated from the fitted model coefficients based according to the desired constitutive model. For the power-law and Ellis models, the volumetric flow rates are respectively calculated as a function of the pressure (QP relations) as:

$$\widehat{Q}(t) = (\pi m R^3 (3 + 1/m) / (1 + 3m)) (P(t) / (2k L \exp(C/T)))$$
(19)

$$\widehat{Q}(t) = \left(\pi R^4 P(t) / (8kL \exp(C/T))\right) (1 + 4/(3 + \alpha)) \left(RP(t) / (2L\tau_{1/2})\right)^{\alpha - 1}$$
(20)

The volumetric flow rate is also computed for the Cross model based on a recently developed integral expression of the local velocity profile [19–21]. In this solution approach, the wall shear rate,  $\dot{\gamma}(t)$ , is first found to equilibrate the wall shear stress based on the pressure drop through the nozzle bore:

$$\underset{\dot{\mathbf{x}}_{-}(t)}{\operatorname{argmin}} \tau_{w}(\dot{\mathbf{y}}_{w}(t)) - \frac{R}{2} \frac{P(t)}{L} \tag{21}$$

where the wall shear stress,  $\tau_w$ , is defined for the Cross model as:

$$\tau_{w}(\dot{\gamma}_{w}) = \dot{\gamma}_{w} \eta = \dot{\gamma}_{w} a / \left(1 + \left(\frac{a}{\tau^{*}}\right)\right)^{1-n} \tag{22}$$

Then, the integral expression for the flow rate for the Cross model is:

$$\widehat{Q}(\dot{\gamma}_{w}(t)) = \frac{\pi a^{3} R^{3} \dot{\gamma}_{w}^{4}}{\tau_{w}^{3}} \left( \frac{4g^{2} + 2m^{2} - m(2f^{2} + 5f + 3)}{6m^{2}g^{3}} + \frac{m^{2} - 6m + 8}{12m^{2}} {}_{2}F_{1}\left(1, \frac{4}{m}; \frac{m+4}{m}; -f\right) \right)$$
(23)

where a is the zero shear rate viscosity with  $a = k \exp(C/T)$ , m = 1 - n,  $f = (a\dot{\gamma}_w/\tau^*)^m$ , g = 1 + f, and  $_2F_1$  is the ordinary hypergeometric function.

For each viscosity and compressibility model, the model coefficients (e.g., subsets of  $\{k,C,m,\alpha,\tau_{1/2},\tau^*,n,b_{3,\mathrm{m}},b_{4,\mathrm{m}}\}$ ) are initialized to the fitted coefficients found in the prior sections. The sum of squared error, SSE, is solved by constrained optimization using the Matlab function fmincon using the interior point method and tolerance limits of 1e-12. The direct use of the SSE defined in Eq. 14 will fit the viscosity and compressibility models with strong weighting towards the higher flow rate process settings since the errors in the mass flow rates will tend to be proportional to the magnitude of the input volumetric flow rates. As such, more robust model fittings are obtained by minimizing the normalized error at each time step, t, within the time range  $t_{i,1} < t < t_{i,2}$  for each i-th characterization run with varying temperatures,  $T_j$ , and flow rates,  $O_i$ :

$$\underset{\left\{k,C,m,a,\tau_{1/2},\tau^*,n,b_{3,m},\quad b_{4,m}\right\}}{\operatorname{argmin}} \quad SSE = \sum_{i} \sum_{t_{i,1} < t < t_{i,2}} \left( e(t) \bigg/ \left( \frac{Q_i}{v_0} \right) \right)^2 \tag{24}$$

To speed convergence, the lower and upper bounds are respectively set to 0.2–5.0 times the initial estimates of the coefficients, except for the limits for m and n that are set to bounds of (0,1) to ensure shear thinning to Newtonian behavior. Given the good starting coefficient estimates from the prior sections, only about three hundred function evaluations of the SSE per Eq. (24) were required for each model to jointly fit the viscosity and compressibility coefficients from their initial estimates. Computation times varied by model, with the power-law and Ellis model requiring a few seconds while the Cross model required a few hours given the need to find the wall shear stress per Eq. (21) at each of the time steps followed by the evaluation of the flow rate with the hypergeometric function per Eq. (24).

Table 5 provides the initial and final estimates of the jointly fit the viscosity and compressibility coefficients for each constitutive model. In the table, the coefficient of determination,  $R^2$ , is evaluated for the non-

**Table 5**Estimated viscosity model coefficients from the transient pressure of Fig. 5.

Model	Coefficient	Initial estimate	Final estimate
Power-law, arg min <i>SSE</i> per Eq. 23	k [Pa s <sup>2-m</sup> ] C [K] m	8.213e-3 6440 0.6424	3.993e-2 5598 0.6396
	b <sub>3,m</sub> [Pa] b <sub>4,m</sub> [1/K]	1.112e+8 4.789e-3	3.036e+8 2.490e-3
Ellis, arg min SSE per Eq. 23	$R^2$ $k \text{ [Pa s}^{1+\alpha}]$ $C \text{ [K]}$ $\tau_{1/2} \text{ (Pa)}$	0.921 1.666e-6 9974 2.051e+5	0.984 1.341e-6 9919 2.051e+5
	$\alpha$ $b_{3,m}$ [Pa]	2.188 1.112e+8	2.297 2.950e+8
	b <sub>4,m</sub> [1/K]	4.789e-3	1.545e-3
Cross, arg min SSE per Eq. 23	k [Pa s] C [K] τ* [Pa s]	0.924 2.073e-6 9939 2.410e+5	0.993 1.895e-6 9896 2.410e+5
	$n$ $b_{3,m}$ [Pa]	0.40186 1.112e+8	0.3961 2.937e+8
	$b_{4,m} [1/K]$ R <sup>2</sup>	4.789e-3 0.922	1.952e-4 0.994

outlying points (COV<2%) by definition as  $R^2=1-SSE/SSY$ , where SSY is the variance of the inlet mass flow rate that is well-estimated as  $SSY=\sum_t \left(\frac{1}{2}Q_i/\nu_0\right)^2$ . Inspection of the results indicates that in all cases,

the performance of the jointly fit viscosity and compressibility models outperform the separately characterized viscosity and compressibility as previously described. Furthermore, inspection of the results indicates that there are relatively minor modifications to the viscosity model coefficients.

Comparison with the compressibility model coefficients  $b_{3,m}$  and  $b_{4,m}$ of Table 5 with those of Tables 1 and 3 indicate that the joint characterization substantially reduces the compressibility by increasing the bulk modulus via coefficient  $b_{3,m}$ . The compressibility behavior of the jointly derived compressibility and Cross viscosity model is plotted in Fig. 2. This variance in behavior was not unexpected given that the majority of the 79 mm filament length (see Fig. 1) is at much lower temperatures than the temperature of the hot end. As such, the 2.937e + 8 estimate for  $b_{3,m}$  in Table 5 representing the bulk modulus compares well with the 2.419e + 8 estimate for  $b_{3,s}$  first established in Table 1 as the bulk modulus for the solid, generic ABS. The likely explanation for the earlier estimate of the lower value for  $b_{3,m}$  with the blocked nozzle is compliance of the Bowden tube and flexure of the filament within the Bowden tube during the repeated filament retractions and advancements. In hindsight, it is probable that the compression experiments may not have applied enough compression to provide an accurate estimate of the system's compressibility behavior

and that it is coincidence that the results of the blocked nozzle aligned with those of the Tait coefficients for the generic ABS. This hypothesis can be verified by evaluating the compressibility using the rate of change towards the end of compression:

$$\beta(T) = -\frac{1}{V} \frac{dV/dt}{dP/dt} \Big|_{T} \xrightarrow{yields} B = V \frac{\Delta P/\Delta t}{FA} = \frac{L}{F} \frac{\Delta P}{\Delta t}$$

$$= \frac{79 \text{mm}}{1 \text{mm/s}} \frac{0.586 - 0.407 \text{MPa}}{1266.9 - 1266.8 \text{s}} = 1.41e8 \quad Pa$$
(25)

This calculation is implemented in Eq. (25) for the data of Fig. 4 and found to increase the estimate of the bulk modulus B to 1.41e8 Pa. The calculation was similarly repeated and fitted to Eq. (3) with the value of  $b_{3,m}$  increasing to 1.763e + 8, indicating that even more compression is needed to estimate the bulk modulus and compressibility at higher pressures. Even so, underlying causality is consistent with the values of  $b_{3,m}$  in Table 5 and the value of  $b_{3,s}$  in Table 1 in which the compressibility was characterized at much higher pressures. Given the need to choose a set of model coefficients for simulation and control purposes, the results of Table 5 seem satisfactory since the results emulate the behavior of the dynamic system during operation.

Fig. 8 provides a typical result from the jointly fit Ellis viscosity and compressibility models for the experimental design's center-point run with a hot end temperature of  $220\,^{\circ}\text{C}$  and an extruder flow rate of  $2.5\,\text{mm}^3/\text{s}$ . This process condition is quite typical in additive manufacturing by material extrusion, and corresponds to a print speed of  $25\,\text{mm}/\text{s}$  for a road width of  $0.5\,\text{mm}$  and a road height of  $0.2\,\text{mm}$ . As

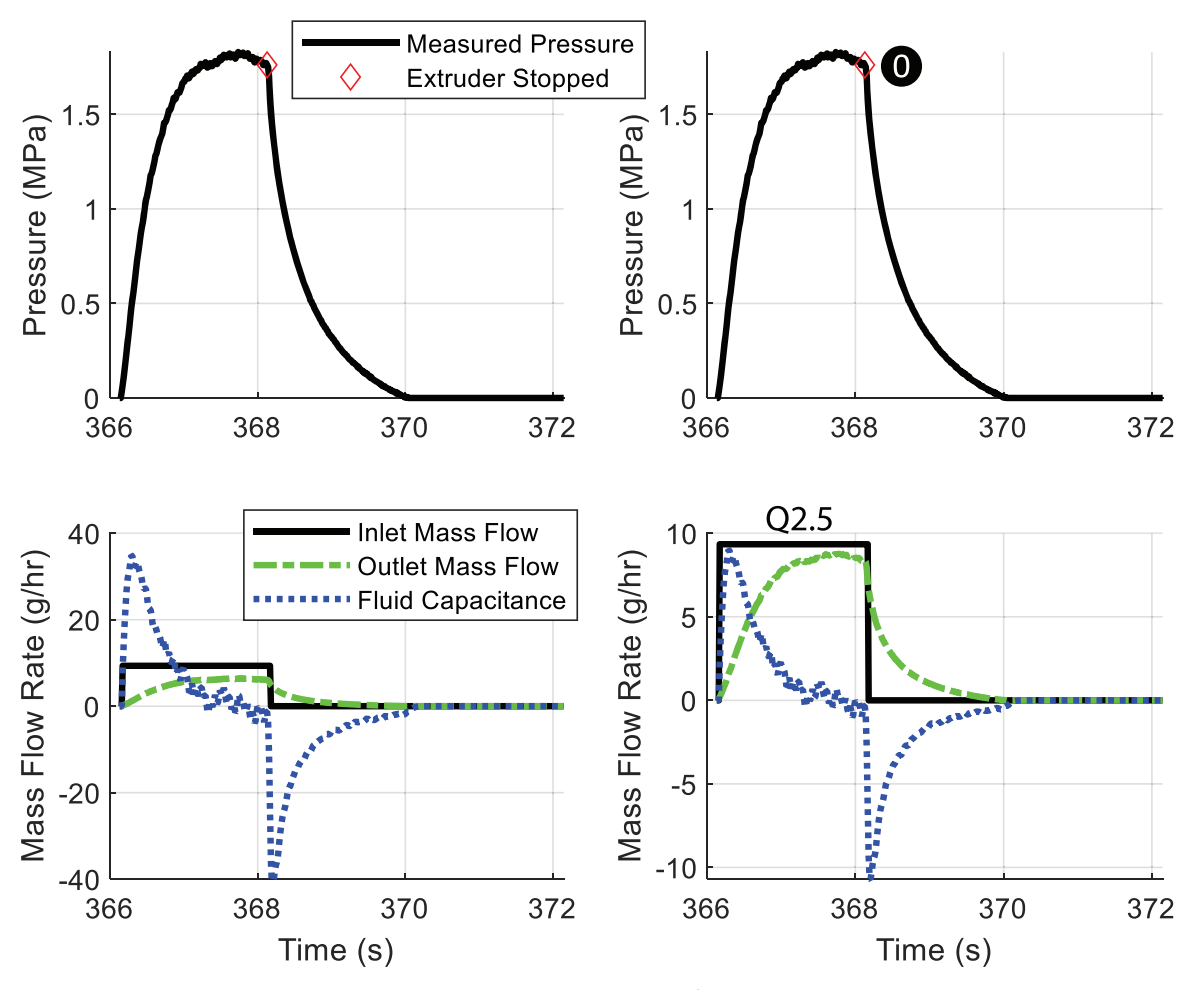


Fig. 8. (top) observed melt pressures for extrusion of ABS at 220 °C and flow rate of 2.5 mm<sup>3</sup>/s, and (bottom) inlet mass flow rates as well as modeled outlet mass flow rate and fluid capacitance from the Ellis viscosity and compressibility models for (left) initial estimates of viscosity and compressibility coefficients from prior sections and (right) jointly fitted coefficients.

**Table 6**Summary of observed conditions, apparent viscosities, and faults.

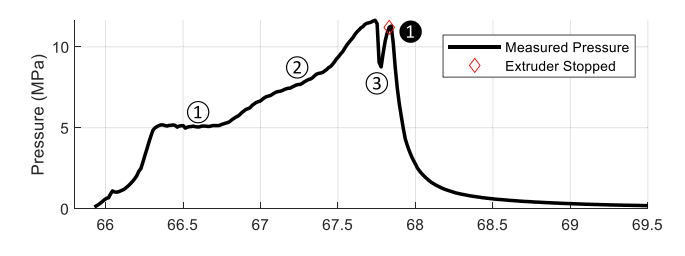
Run	T, °C	Q, uL/s	P, MPa	γ̈, 1/s	$\mu$ , Pa s	COV (%)	Point in Fig. 6	Fault (s)
1	240	20.00	11.642	3183.1	304.8	7.52	0	1, 2
2	240	14.14	6.585	2250.8	243.8	9.81	<b>2</b>	1, 3
3	240	10.00	3.930	1591.5	205.8	7.53	•	1, 3
4	240	7.07	2.700	1125.4	199.9	3.83	•	3
5	240	5.00	2.040	795.8	213.6	0.75		
6	240	3.54	1.733	562.7	256.7	0.50		
7	240	2.50	1.431	397.9	299.7	1.02		
8	240	1.77	1.100	281.4	325.7	0.55		
9	240	1.25	0.787	198.9	329.6	1.13		4
10	240	0.88	0.421	140.7	249.2	2.78		4, 5
11	240	0.63	0.180	99.5	150.9	3.76		4, 5
12	240	0.44	0.085	70.3	100.9	7.10		4, 5
13	240	0.31	0.025	49.7	42.3	23.88		4, 5
22	220	14.14	8.202	2250.8	303.7	7.50		1, 3
23	220	10.00	5.771	1591.5	302.2	3.43		1, 3
24	220	7.07	4.245	1125.4	314.3	0.23		3
25	220	5.00	3.248	795.8	340.2	0.27		3
26	220	3.54	2.640	562.7	391.0	0.27		
27	220	2.50	2.185	397.9	457.6	0.33	0	
28	220	1.77	1.829	281.4	541.8	0.58		
29	220	1.25	1.435	198.9	600.9	0.90		4
30	220	0.88	1.112	140.7	658.6	1.94		4
31	220	0.63	0.841	99.5	705.0	1.85	6	4, 5
32	220	0.44	0.572	70.3	677.5	3.33	6	4, 5
33	220	0.31	0.338	49.7	566.8	6.00	0	4, 5
34	220	0.22	0.124	35.2	294.0	11.18	•	4, 5
42	200	10.00	8.360	1591.5	437.8	0.01		1
43	200	7.07	7.117	1125.4	527.0	0.05		1
44	200	5.00	5.683	795.8	595.1	3.76		
45	200	3.54	4.380	562.7	648.6	0.23		
46	200	2.50	3.617	397.9	757.6	0.34		
47	200	1.77	3.052	281.4	903.9	0.54		
48	200	1.25	2.533	198.9	1060.9	0.27		
49	200	0.88	2.069	140.7	1225.7	0.26		4
50	200	0.63	1.613	99.5	1351.5	0.20		4
51	200	0.44	1.245	70.3	1474.6	1.72		4
52	200	0.31	0.948	49.7	1587.6	1.98		4
53	200	0.22	0.573	35.2	1357.8	4.08		4
54	200	0.16	0.516	24.9	1729.1	4.79		4

observed by the left subplots in Fig. 8, the initially derived viscosity and compressibility model coefficients come close to predicting the steady state flow rate given the observed pressure but significantly over predict the fluid capacitance at the start and stopping of the extrusion. By comparison, the final viscosity and compressibility coefficients elucidate the underlying physics. At the start of the extrusion, there is a significant delay in the output mass flow rate as the fluid capacitance builds. Afterwards, the steady state mass flow rate closely matches the extruder mass flow rate. Finally, after the extruder is stopped, the output mass flow rate is provided by the decrease in the fluid capacitance.

The behaviors across the 39 runs of varying flow rates and temperatures are qualitatively similar that observed in Fig. 8, but there are significant differences in behavior. For those readers interested in the individual process and model behaviors, a set of 242 plots similar to Fig. 8 is provided in the supplemental materials corresponding to each of the 39 runs, for incompressible and compressible model coefficients, and the power-law, Ellis, and Cross models. The results suggest that the concurrent characterization of viscosity and compressibility is highly capable and yields reasonable constitutive model coefficients. However, there are some significant variances between the model results and observed behaviors. These variances are largely due to the invalidity of standard assumptions in view of unexpected process faults, which are now discussed.

## 6. Fault diagnoses and discussion

Each of the 39 sets of transient melt pressure data were extensively reviewed. Table 6 provides a summary of the observed behaviors of the



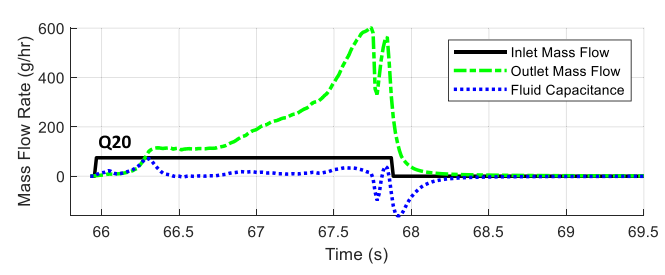
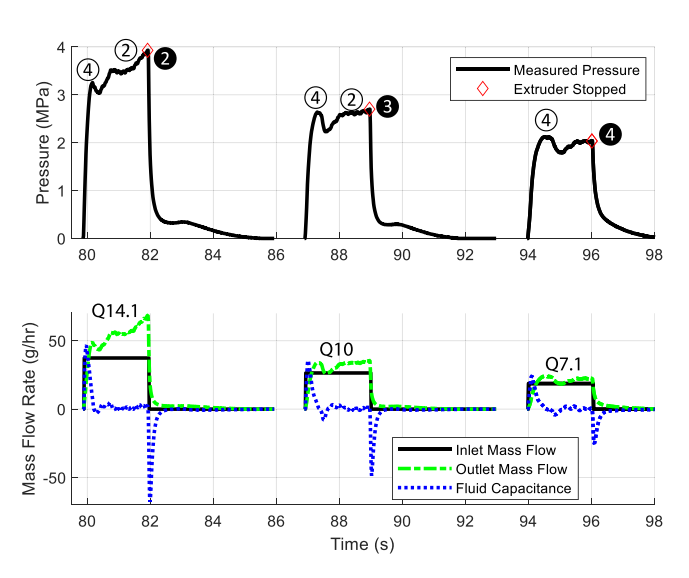


Fig. 9. (top) observed melt pressures for extrusion of ABS at 240  $^{\circ}$ C and flow rate of 20 mm<sup>3</sup>/s, and (bottom) inlet mass flow rates as well as modeled outlet mass flow rate assuming isothermal melt flow.

dynamic data and fitted models plotted in the supplementary materials. Several different faults were identified as subsequently discussed that explain the observed variances in the melt pressure and modeled viscosity behavior such as those marked with an "x" in Fig. 7. The underlying causes are consistent with polymer processing theory and are

coded in Table 6 as (1) limited melting capacity of the hot end, (2) skipping (grinding) of the extruder drive gears, (3) low initial nozzle temperature, (4) varying flow rates associated with the intermeshing gear tooth velocity profile, and (5) delays and reduced melt pressures due to drool prior to extrusion. The details of these phenomena are obvious in hindsight but have not been previously diagnosed via pressure measurement.

1. Limited melting capacity of the hot end: Fig. 9 provides the observed melt pressure for extrusion of ABS at 240 °C and an extruder flow rate of 20 mm<sup>3</sup>/s, which corresponds to point **0** in Fig. 7. This flow rate is much greater than typical extrusion, corresponding to a print speed of 200 mm/s (12,000 mm/min) for a road having a width and height of 0.5 and 0.2 mm, respectively. The pressure data of Fig. 9 shows that the melt initially obtains an equilibrium at ① with the viscosity model fairly accurately predicting the viscosity and mass flow rate as a function of the observed pressure. However, continued high mass flow rates draw significant heat from the hot end, such that the melt temperature drops and the melt pressure begins to increase significantly at ②. This increased melt pressure corresponds to the higher apparent viscosity at point **0** as compared to point **9** in Fig. 7. ABS is a shear thinning fluid, so a decreased viscosity would be expected for increased shear rate under isothermal conditions as shown for all of the viscosity models in Fig. 7. However, at high flow rates such as at point **0** (as well as points 2 and 3) there is insufficient heat conduction from the hot end to the melt, causing a decrease in the melt temperature and an increased melt pressure and apparent viscosity. These results are consistent with finite element analysis of heat transfer within the hot end [22], which found that increasing the extruder flow rate from 8.33 mm<sup>3</sup>/s to 25 mm<sup>3</sup>/s decreased the core temperature by approximately 150 °C for an extruder setpoint of 260 °C. The pressure and viscosity at point **0** are artificially high because of the lower temperature – this point is further supported by the calculated mass flow rate given in Fig. 9. In the initial equilibrium at ①, the inlet and outlet flow rates are nearly the same, which is the expected behavior; however, the calculated outlet mass flow rate more than doubles as the melt pressure increases. Supplemental material 2b provides plots of pressure and flow rate in the style of Fig. 9 for all runs plotted in Fig. 7.



**Fig. 10.** (top) observed melt pressures for extrusion of ABS at 240  $^{\circ}$ C and flow rate of 14.1, 10, and 7.1 mm³/s corresponding to points **②**, **③**, and **④** in Fig. 7, and (bottom) inlet mass flow rates as well as modeled outlet mass flow rate assuming isothermal melt flow.

- 2. Skipping (grinding) of the extruder drive gears: With further increased pressure in the melt pressure after ② in Fig. 9, a plateauing of the pressure is observed as the filament drive system stalls and ultimately skips at ③. The temporary reduction in the flow rate allows the melt temperature in the hot end to rise, thereby reducing the pressure until the melt begins to cool again. This behavior of melting and skipping was observed in the injection printing process with divots appearing in the injection in the cavities between the shell walls [23]; that paper explains the need for greater melting capacity in order to increase production speeds with additive manufacturing by material extrusion. While the transient data is helpful to characterize the melting capacity of hot ends and required drive torque, further research is planned to model the dynamic melt temperature using a modeling methodology similar to that implemented for melt flows in hot runners of injection molding [24].
- 3. Low initial nozzle temperature: Fig. 10 plots the observed melt pressures for the next three experimental runs at 240 °C corresponding to flow rates of 14.1, 10, and 7.1 mm<sup>3</sup>/s. In each of the three cases, the melt pressure is observed to overshoot the steady melt pressure at 4. While it is possible that this pressure is caused by stress overshoot related to the entanglement of polymer networks [25,26], it is believed to be more likely caused by lower temperatures of the melt in the bore of the nozzle. Specifically, there is a 5 s delay between the extruder stoppage and the next start for characterization of the next flow rate. The cooling fan is constantly directing air over the hot end with a focus on the nozzle tip. As such, it is likely that the nozzle tip (with only indirect heating from its threaded engagement with the hot end) would cool and require higher initial melt pressures to clear. Furthermore, the time span of the overshoot increases with lower flow rates, which is consistent with the lower rates of melt convection at lower flow rates.

Fig. 10 at 3 also demonstrates the inadequate melting capacity at flow rates of 14.1 and  $10~\text{mm}^3/\text{s}$ . In these cases, there is an increase in the melt pressure that results in an overprediction of the mass flow rate that is due to decreased melt temperatures. The slope of the melt pressure at 9 for a flow rate of 14.1 mm $^3/\text{s}$  suggests that this flow rate is not sustainable and would likely result in intermittent skipping of the drive gear. The melt pressure at 9 for a flow rate of  $10~\text{mm}^3/\text{s}$  would likely be sustainable but could result in decreased extrudate melt temperatures

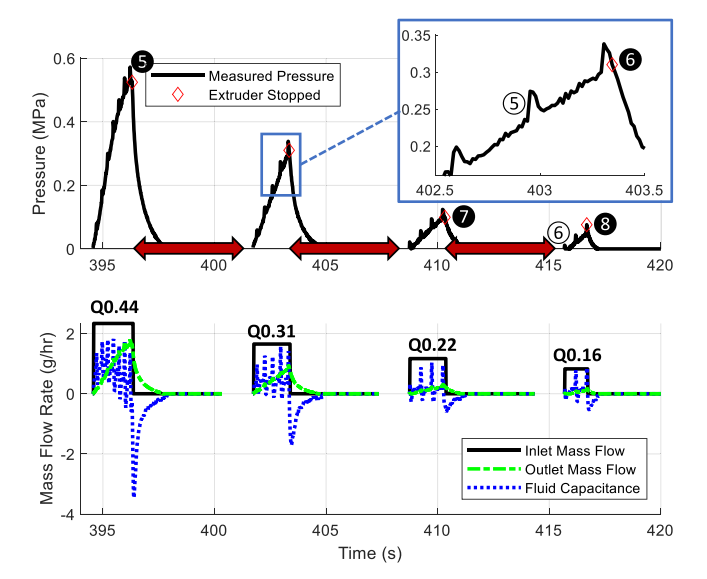


**Fig. 11.** (top) observed melt pressures for extrusion of ABS at 240  $^{\circ}$ C and flow rate of 0.44, 0.31, 0.22, and 0.15 mm<sup>3</sup>/s corresponding to points  $\Theta$ ,  $\Theta$ ,  $\Theta$ , and  $\Theta$  in Fig. 7, and (bottom) inlet mass flow rates as well as modeled outlet mass flow rate assuming isothermal melt flow.

that could decrease the bond strength of the deposited roads.

- 4. Varying flow rates associated with the intermeshing gear tooth velocity profile: The instrumented hot end has a theoretical pressure resolution of  $\delta P = 13 \text{MPa}/2^{16} = 0.0002 \text{MPa}$ . The use of the word "theoretical" in the preceding sentence is intended to suggest a best case scenario in the absence of electrical noise, viscous drag between the melt sensor pin and sensing bore of the hot end, mechanical vibration and acceleration effects, and other potential issues. While the true melt pressure resolution is unknown, the melt pressure measurement is certainly good enough to identify the occurrence of varying flow rates associated with gear tooth velocity as shown in Fig. 11. Specifically, the drive gears for the Micro Swiss direct drive extruder have 18 teeth spaced about a 10 mm diameter. At low flow rates, the intermeshing of the drive gears causes a nonuniform velocity profile [27] of the driven filament as evident in the melt pressures at ⑤ in Fig. 11. These melt pressure impulses are very repeatable and observable across a surprisingly broad range of flow rates – even the melt pressures plotted in Fig. 10 at high flow rates indicate the presence of high frequency pressure variation for the same reason. Fortunately, the bulk of the flow rate variation is absorbed by the fluid capacitance of the material being processed. However, some of this imbued flow rate variation is likely transmitted to the deposited roads as predicted in the outlet mass flow rates in Fig. 11 and can cause variations in surface finish and other part properties at low flow rates.
- 5. Delays and reduced melt pressure due to drool prior to extrusion: The red arrows at the bottom of Fig. 11 represent the 5 s delay between the extruder stoppage and the start of the next characterization cycle; the left end of each arrow is aligned with the diamond representing the stoppage of the extruder. The start of the extrusion should coincide with the right side of each red arrow. However, there is delay until melt pressures are observed at lower flow rates such as <a>©</a>. The delay increases with decreasing flow rate and is likely caused by melt drool from the nozzle during the 5 s of idle time. Accordingly, the volume of the flow channels inside the hot end must refill with melt before a positive melt pressure is observed. Furthermore, the lack of melt densification prevents the realization of steady state flow rates that causes the reduced apparent viscosities at points <a>©</a>, and <a>©</a> in Fig. 7.

#### 7. Conclusion

The research has established the feasibility for characterizing both the viscosity and compressibility behavior of material using an instrumented hot end for additive manufacturing by material extrusion. The authors have not implemented Bagley end corrections [28-30] or the Weissenberg-Rabinowitsch shear rate corrections [31] since viscosity and compressibility behavior can be quickly characterized as described for any specific material/nozzle combination and so the underlying complicating phenomena are reflected by the behavior of the material processed in the apparatus and so empirically modeled to known statistical fidelity. Still, the derived model coefficients reflect the observed system behavior and should provide better simulation and control results than more sophisticated models that remove these effects, only then needing to add them back in with additional models to try and reconstitute the complex system behavior. The described modeling methodology was found to be highly effective and so will also be applied to explain transient variances observed in capillary rheology [32] that are now believed to be related to compressibility.

The issues of melt flow rate, pressure, and temperature variations are clearly significant and need to be modeled and controlled to achieve higher production speeds and improved product quality. Indeed, the most critical issue in application of in-line characterization of viscosity and compressibility is the confounding between variations in melt temperature and melt pressure. The presented results suggest that the

range of quasi-isothermal processing is quite broad, certainly valid for volumetric flow rates less than 5 cubic millimeters/s for this hot end design. Standard hot ends will not perform as well, and Osswald [33] suggests that there is often a very abrupt temperature transition at higher flow rates. For this reason, further research is recommended that implements internal infrared pyrometry to further study the melting dynamics and adiabatic heating as a function of flow rate [34].

Even so, the use of the instrumented hot end has led to vital insights into the underlying processing physics. The increased observability of the process can be used to reliably detect and compensate for processing faults in real time to such an extent that such instrumentation should be universally applied in production systems and critical applications to ensure that additively manufactured products by material extrusion are born qualified [35].

#### Supplemental Materials

Supplemental materials include the data for the blocked and open nozzle experiments. Also provided are transient pressure and flow rate plots (similar to Fig. 9) of the compressible flow fitting for the power-law, Ellis, and Cross models for all 39 experimental runs.

#### CRediT authorship contribution statement

**David O. Kazmer:** Conceptualization, Formal analysis, Methodology, Software, Validation, Writing - original draft. **Austin R. Colon:** Validation, Writing - review & editing. **Amy M. Peterson:** Conceptualization, Writing - review & editing. **Sun Kyoung Kim:** Formal analysis, Writing - review & editing.

#### **Declaration of Competing Interest**

The authors declare that they have no known competing financial interests or personal relationships that could have appeared to influence the work reported in this paper.

#### Acknowledgements

Portions of this work is based upon work supported by the National Science Foundation under Grant No. #1914651. Any opinions, findings, and conclusions or recommendations expressed in this material are those of the author(s) and do not necessarily reflect the views of the National Science Foundation. The first author was one of General Electric's representatives to the Cornell Injection Molding Program from 1990 to 1992 and thanks KK Wang as well as all the CIMP researchers for providing a vision that was central to his career and the tenets of this research; this author also recognizes C.A. (Neil) Heiber's 1980 Fortran program Simplex1D to fit non-isothermal, non-Newtonian viscosity models from capillary rheometer data that provided a modeling paradigm for this specific work.

## Appendix A. Supporting information

Supplementary data associated with this article can be found in the online version at doi:10.1016/j.addma.2021.102106.

## References

- [1] 2020, "Autodesk/Moldflow materials database for generic ABS."
- [2] H. Chiang, C. Hieber, K. Wang, A unified simulation of the filling and postfilling stages in injection molding. Part I: formulation, Polym. Eng. Sci. 31 (2) (1991) 116–124.
- [3] Hwai Hai Chiang, "Simulation and Verification of Filling and Post-Filling Stages of the Injection Molding Process," PhD Dissertation, Mechanical Engineering, Cornell University, Ithaca, NY, 1989.
- [4] T.J. Coogan, D.O. Kazmer, In-line rheological monitoring of fused deposition modeling, J. Rheol. 63 (1) (2019) 141–155.

- [5] T.J. Coogan, D.O. Kazmer, Modeling of interlayer contact and contact pressure during fused filament fabrication, J. Rheol. 63 (4) (2019) 655–672.
- [6] R.R. Panchal, D. Kazmer, "Characterization of polymer flows in very thin gaps," in International Manufacturing Science and Engineering Conference, 2007, vol. MSEC2007-31108, pp. 179–189.
- [7] J. Dymond, R. Malhotra, The Tait equation: 100 years on, Int. J. Thermophys. 9 (6) (1988) 941–951.
- [8] G.A. Neece, D.R. Squire, Tait and related empirical equations of state, J. Phys. Chem. 72 (1) (1968) 128–136.
- [9] P. Tait, Physics and chemistry of the voyage of HMS challenger, Sci. Pap. 2 (1888).
- [10] P. Zoller, The pressure–volume–temperature properties of three well-characterized low-density polyethylenes, J. Appl. Polym. Sci. 23 (4) (1979) 1051–1056.
- [11] P. Zoller, A study of the pressure-volume-temperature relationships of four related amorphous polymers: polycarbonate, polyarylate, phenoxy, and polysulfone, J. Polym. Sci. Polym. Phys. Ed. 20 (8) (1982) 1453–1464.
- [12] P. Zoller, D.J. Walsh, Standard Pressure-Volume-Temperature Data for Polymers, CRC Press, 1995.
- [13] D.O. Kazmer, C.M. Grosskopf, D. Rondeau, V. Venoor, Design and evaluation of general purpose, barrier, and multichannel plasticating extrusion screws, Polym. Eng. Sci. 60 (4) (2020) 752–764.
- [14] D. Kazmer, Injection Mold Design Engineering, second ed., Carl Hanser Verlag, Munich, 2016, p. 410.
- [15] M.L. Williams, R.F. Landel, J.D. Ferry, The relaxation distribution function of polyisobutylene in the transition from rubber-like to glass-like behavior, J. Appl. Phys. 24 (1953) 911–916.
- [16] J.D. Ferry, Viscoelastic Properties of Polymers, third ed., Wiley, New York, 1980.
- [17] E. Mitsoulis, O. Delgadillo-Velazquez, S.G. Hatzikiriakos, Transient capillary rheometry: compressibility effects, J. Non-Newton. Fluid Mech. 145 (2–3) (2007) 102-108
- [18] B.T. Kulakowski, J.F. Gardner, J.L. Shearer, Fluid systems. Dynamic Modeling and Control of Engineering Systems, Cambridge University Press, 2007, pp. 219–244.
- [19] T. Sochi, Using the Euler-Lagrange variational principle to obtain flow relations for generalized Newtonian fluids, Rheol. Acta 53 (1) (2014) 15–22.
- [20] T. Sochi, Analytical solutions for the flow of Carreau and Cross fluids in circular pipes and thin slits, Rheol. Acta 54 (8) (2015) 745–756.

- [21] S.K. Kim, Flow-rate based method for velocity of fully developed laminar flow in tubes, J. Rheol. 62 (6) (2018) 1397–1407.
- [22] J. Go, S.N. Schiffres, A.G. Stevens, A.J. Hart, Rate limits of additive manufacturing by fused filament fabrication and guidelines for high-throughput system design, Addit. Manuf. 16 (2017) 1–11.
- [23] D.O. Kazmer, A. Colon, Injection printing: additive molding via shell material extrusion and filling, Addit. Manuf. 101469 (2020).
- [24] B. Fan, D.O. Kazmer, R. Nageri, An analytical non-Newtonian and nonisothermal viscous flow simulation, Polym. -Plast. Technol. Eng. 45 (3) (2006) 429–438.
- [25] Y. Lu, L. An, S.-Q. Wang, Z.-G. Wang, Origin of stress overshoot during startup shear of entangled polymer melts, ACS Macro Lett. 3 (6) (2014) 569–573.
- [26] K. Osaki, T. Inoue, T. Isomura, Stress overshoot of polymer solutions at high rates of shear, J. Polym. Sci. Part B Polym. Phys. 38 (14) (2000) 1917–1925.
- [27] D. Yang, Z. Sun, A rotary m odel for spur gear dynamics, J. Mech. Des. 107 (4) (1985) 529–535.
- [28] E. Bagley, End corrections in the capillary flow of polyethylene, J. Appl. Phys. 28 (5) (1957) 624–627.
- [29] M. Dees, M. Mangnus, N. Hermans, W. Thaens, A.-S. Hanot, P. Van Puyvelde, On the pressure correction of capillary melt rheology data, Rheol. Acta 50 (2) (2011) 117–124.
- [30] E. Mitsoulis, S. Hatzikiriakos, K. Christodoulou, D. Vlassopoulos, Sensitivity analysis of the Bagley correction to shear and extensional rheology, Rheol. Acta 37 (5) (1998) 438–448.
- [31] C. Hieber, H. Chiang, Shear-rate-dependence modeling of polymer melt viscosity, Polym. Eng. Sci. 32 (14) (1992) 931–938.
- [32] A. Moshe, D. Kazmer, S. Johnston, R. Malloy, S. Kenig, Analysis of variance in capillary rheometry, Polym. Eng. Sci. 56 (8) (2016) 895–904.
- [33] T.A. Osswald, J. Puentes, J. Kattinger, Fused filament fabrication melting model, Addit. Manuf. 22 (2018) 51–59.
- [34] C. Luo, X. Wang, K.B. Migler, J.E. Seppala, Effects of feed rates on temperature profiles and feed forces in material extrusion additive manufacturing, Addit. Manuf. 35 (2020), 101361.
- [35] R.A. Roach et al., "Born qualified grand challenge LDRD final report," Sandia National Lab.(SNL-NM), Albuquerque, NM (United States), 2018.